THE JOURNAL OF CELL BIOLOGY

An alternative mechanism of clathrin-coated pit closure revealed by ion conductance microscopy

Andrew I. Shevchuk,[1,2] Pavel Novak,[1,3] Marcus Taylor,[4] Ivan A. Diakonov,[3] Azza Ziyadeh-Isleem,[5,6] Marc Bitoun,[7] Pascale Guicheney,[5,6] Max J. Lab,[3] Julia Gorelik,[3] Christien J. Merrifield,[8] David Klenerman,[9] Yuri E. Korchev[1]

[1]Division of Experimental Medicine, Department of Medicine, Imperial College London, London W12 0NN, England, UK
[2]The Institute For Life Sciences, University of Southampton, Southampton SO17 1BJ, England, UK
[3]Department of Cardiovascular Sciences, National Heart and Lung Institute, Imperial College London, London SW3 6LY, England, UK
[4]Medical Research Council Laboratory of Molecular Biology, Cambridge CB2 2QH, England, UK
[5]Institut National de la Santé et de la Recherche Médicale, UMRS 956, Fondation ICAN, Paris, Cedex 13, France
[6]Université Pierre et Marie Curie, 75005 Paris, France
[7]UMR S974 Université Pierre et Marie Curie, U974 Institut National de la Santé et de la Recherche Médicale, UMR 7215 Centre National de la Recherche Scientifique, Institut de Myologie, 75013 Paris, France
[8]Laboratoire d'Enzymologie et Biochimie Structurales, Centre de Recherche de Gif, Centre National de la Recherche Scientifique, 91190 Gif-sur-Yvette, France
[9]Department of Chemistry, University of Cambridge, Cambridge CB2 1EW, England, UK

Current knowledge of the structural changes taking place during clathrin-mediated endocytosis is largely based on electron microscopy images of fixed preparations and x-ray crystallography data of purified proteins. In this paper, we describe a study of clathrin-coated pit dynamics in living cells using ion conductance microscopy to directly image the changes in pit shape, combined with simultaneous confocal microscopy to follow molecule-specific fluorescence. We find that 70% of pits closed with the formation of a protrusion that grew on one side of the pit, covered the entire pit, and then disappeared together with pit-associated clathrin–enhanced green fluorescent protein (EGFP) and actin-binding protein–EGFP (Abp1-EGFP) fluorescence. This was in contrast to conventionally closing pits that closed and cleaved from flat membrane sheets and lacked accompanying Abp1-EGFP fluorescence. Scission of both types of pits was found to be dynamin-2 dependent. This technique now enables direct spatial and temporal correlation between functional molecule-specific fluorescence and structural information to follow key biological processes at cell surfaces.

Introduction

Clathrin-mediated endocytosis (CME) starts with the formation of nanoscale pits, which then form a vesicle and transport cargo into the cell. EM images of coated structures of various curvatures and sizes, ranging from 60 to 120 nm, found on the cytoplasmic side of the cell membrane have created a picture of the structural changes that take place during CME (Heuser, 1980; Pearse and Crowther, 1987). However, these experiments provided only snapshots of pit formation, closure, and scission. Various forms of fluorescent microscopy such as epifluorescence, confocal, and total internal reflection fluorescence (TIRF) have been used to follow the dynamics of CME in live cells with high temporal resolution and diffraction-limited optical resolution (Gaidarov et al., 1999; Rappoport and Simon, 2003; Merrifield, 2004; Merrifield et al., 2005; Taylor et al., 2011). By labeling different molecules and following how their fluorescence changes, it has been possible to build up a picture of the time course of the major events taking place during CME (Merrifield et al., 2002, 2005; Rappoport, 2008). Until now, it has not been possible to establish a direct link between fluorescence and the structures formed at the cell membrane because the visualization of the cell membrane topography by fluorescence techniques remains challenging, and the need for combined fluorescence and EM studies has been highlighted (Kaksonen et al., 2006). Although recently, the nanometer-scale localization of proteins in electron micrographs was achieved using correlative

Correspondence to Andrew I. Shevchuk: a.shevchuk@soton.ac.uk; or Yuri E. Korchev: Y.Korchev@imperial.ac.uk

Abbreviations used in this paper: CCP, clathrin-coated pit; CCS, clathrin-coated structure; CME, clathrin-mediated endocytosis; HPICM, hopping probe ICM; ICM, ion conductance microscopy; SICM, scanning ICM; TEM, transmission EM; TIRF, total internal reflection fluorescence; WT, wild type.

The Rockefeller University Press $30.00
J. Cell Biol. Vol. 197 No. 4 499–508
www.jcb.org/cgi/doi/10.1083/jcb.201109130

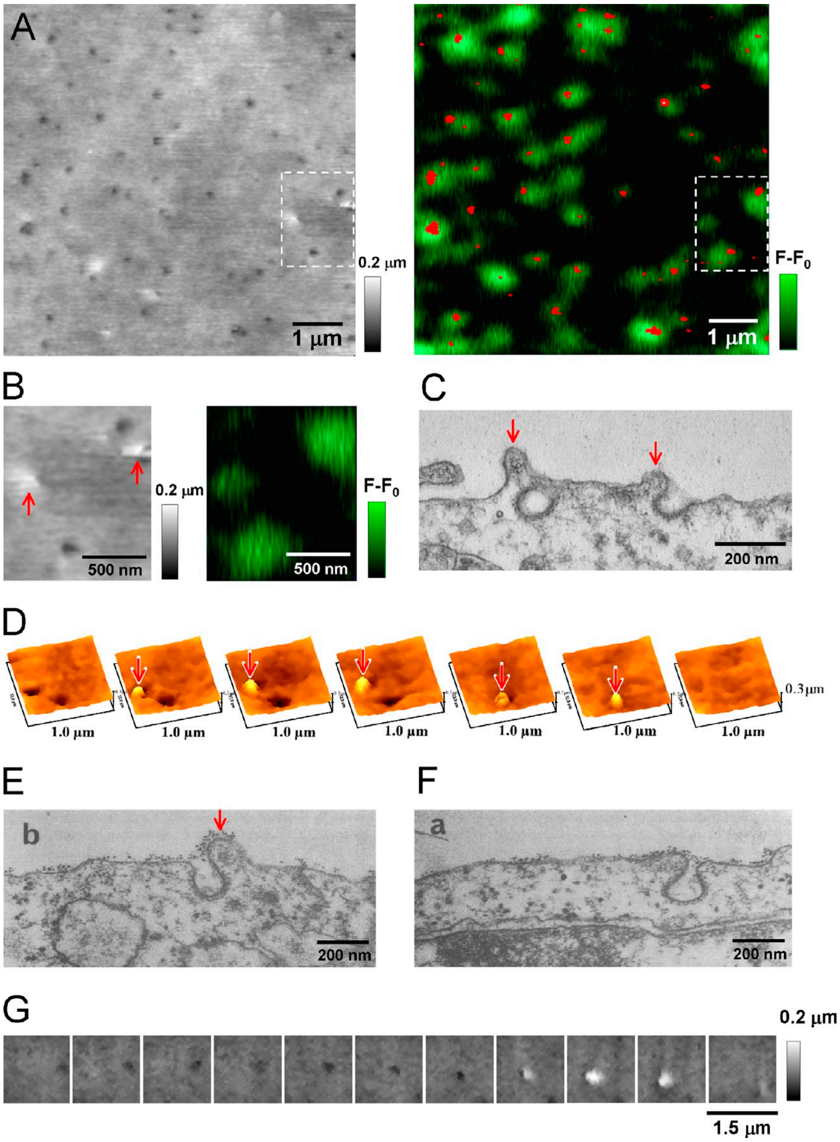

Figure 1. **Imaging of CCPs by combined ICM and confocal microscopy and TEM.** (A) Topographical image of a fixed Cos-7 cell (left) and corresponding fluorescent image (right) of the same clathrin-EGFP–transfected cell superimposed onto the topographical image but inverted and presented in a red palette, as previously described (Shevchuk et al., 2008). The image reveals that the pit topography matches the Clc-EGFP fluorescence. (B) Zoomed topographical and fluorescent images of the areas boxed in A show clathrin fluorescent signal associated with the protrusions on the cell surface. (C) TEM image of cell plasma membrane protrusion associated with a CCP in the Cos-7 cell. (D) A sequence of HPICM topographical images shows the formation of a protrusion before CCP closure in a Cos-7 cell. (E) A TEM image shows the protrusion of cell plasma membrane associated with CCP in an NIH 3T3 cell. (B–E) Red arrows point at membrane protrusions associated with CCPs. (F) A TEM image shows a CCP without distinct protrusion in an NIH 3T3 cell. (E and F) TEM images were reproduced with permission from Bretscher et al. (1980). (G) The sequence of HPICM topographical images shows CCP closure with the formation of a protrusion in an NIH 3T3 cell.

fluorescence EM, this method still remains limited to fixed samples (Watanabe et al., 2011).

Ion conductance microscopy (ICM) can obtain complementary information about CME by the direct label-free measurement of the structures formed at the cell surface over the entire lifetime of clathrin-coated pits (CCPs). Scanning ICM (SICM) was first used to image polymer films (Hansma et al., 1989) but was later shown to be useful for nanoscale imaging of live cells (Korchev et al., 1997a,b). Combined with laser confocal microscopy, ICM is a powerful method for correlative fluorescence and topography imaging (Shevchuk et al., 2008). Recent advances in ICM, which include improved topographical resolution (Shevchuk et al., 2006) and the invention of hopping probe ICM (HPICM; Novak et al., 2009), have brought the quality of ICM imaging to levels comparable with scanning EM, however, retaining live-cell imaging capabilities. We have now improved the temporal resolution of ICM to follow the dynamics of coated pits in live cells.

Results and discussion

Imaging CCP closure in fixed and live cells

We have previously used SICM combined with fluorescence confocal microscopy to image CCPs in the apical membrane of fixed Cos-7 cells and shown that topographically detected pits colocalized with clathrin light chain–EGFP (Clc-EGFP; Shevchuk et al., 2008). Similar densities of CCPs were found in Cos-7 cells by other researchers (Zoncu et al., 2007). A more detailed analysis of images obtained on fixed cells showed that not only topographically detected pits (Fig. 1 A) but also membrane protrusions were associated with Clc-EGFP (Fig. 1 B, red arrows). We studied CCPs in Cos-7 cells fixed at 37°C using transmission EM (TEM) and found that indeed membrane protrusions could be seen in 18 out of 55 identified CCPs (Fig. 1 C, red arrows). Continuous ICM imaging of living Cos-7 cells at 28°C has shown that these protrusions directly relate to CCPs and appeared before pit closure (Fig. 1 D [red arrows] and Video 1). Despite ample examples of EM images in the published literature that do not show CCP-associated protrusions, structures protruding at one side of the pit were previously shown by other researchers using TEM images of mouse fibroblast line NIH 3T3 cells fixed at 22°C (Fig. 1 E, red arrow; Bretscher et al., 1980), BSC1 cells fixed at room temperature (Macia et al., 2006), cultured B lymphoblastoid cells fixed at room temperature (Salisbury et al., 1980), and human fibroblasts fixed at 4°C (Anderson et al., 1976). For comparison, a CCP without a protrusion is shown in Fig. 1 F (Bretscher et al., 1980). Using live ICM imaging, we confirmed that the formation of a protrusion before pit closure can be seen in live NIH 3T3 cells (Fig. 1 G), and it is not specific to the Cos-7 cell type.

ICM imaging of CCPs in living cells was performed at 28°C because the dynamics of CCPs at 37°C is too rapid to get accurate measurements as a result of the limited scan rate of the existing ICM setup. A similar approach of reducing the temperature of observation was previously described (Wu et al., 2001). Although lower than the mammalian core temperature of 37°C, this temperature is close to the lower limits of peripheral temperature in humans during the circadian cycle (∼30°C; Lack and Gradisar, 2002). To test that the formation of protrusions is not the result of lowering the temperature to 28°C, we performed control experiments and confirmed that protrusions also form at 37°C (Fig. S1 A). The mean lifetime of a pit at 37°C calculated on the basis of HPICM images is 54.6 ± 3.7 s ($n = 93$), which is in a good agreement with previously published findings (Loerke et al., 2009; Mettlen et al., 2009).

We used TIRF microscopy to characterize the dynamics of CME in Cos-7 cells under identical conditions to those used for ICM (28°C) and observed scission events and productive internalization (Fig. S1 [B–E] and Video 2). Using automated multiparticle tracking, we found the mean lifetime of pits associated with scission events was significantly longer than the lifetime of those clathrin-coated structures (CCSs) that were not associated with scission events (185 vs. 44 s; $P < 0.05$, calculated using the Student's t test and assuming equal variance). The mean time between nucleation of a CCS and the first detected scission event was 102 s (Fig. S1, F and G). These estimates of CCS lifetime were confirmed by detailed analysis of a manually curated subset of tracking data (Fig. S1, H and I), and the CCS lifetimes measured using TIRF were in good agreement with the lifetime measured by ICM (see Fig. 3 [F and H]). The lifetime of pits with scission events (184 s) is longer than the lifetime between nucleation of a CCS and the first scission event (102 s) because CCS can persist after hosting a scission event and may host subsequent events. The more detailed analysis was previously described (Merrifield et al., 2005; Taylor et al., 2011). Although longer than previously published lifetimes at 37°C (Loerke et al., 2009; Mettlen et al., 2010), our results are in good agreement with the observation that at 28°C, transferrin uptake is decreased by a factor of four, as compared with 37°C (Wu et al., 2001).

We further characterized the entire life cycle of single CCPs in Cos-7 cells by simultaneous HPICM topographical and fluorescent imaging at rates varying from 7 to 17 s per frame. We observed an initiation phase during which the diameter and depth of pits enlarged followed by a steady-state phase and closure. The total number of pits analyzed was 215, including 70 pits that drifted in or out of the area of observation before closure and therefore were not included in lifetime, formation, and closure statistics. In 101 cases out of 145, pit closure was associated with the formation of a side protrusion above the cell membrane, which we will refer to as a cap, and 44 pits closed without cap formation.

Analysis of CCPs that close with protrusion (cap)

Fig. 2 A shows detailed topographic changes during the pit closure associated with the formation of the cap, which initially appears beside the pit and then covers the whole pit before it disappears. The sequence of topographical and fluorescent image pairs shown in Fig. 2 B represents a typical pit that closes with a cap (Fig. 2 B, red circles). Note that Clc-EGFP fluorescence disappears simultaneously with the disappearance of the cap and pit. A similar CME event is shown in Video 3. The slight offset of topographically detected pits relative to the clathrin-GFP fluorescence spots is a result of the residual misalignment and/or the drift of the ICM imaging probe (nanopipette) relative to the laser beam.

By analyzing time-lapse recordings, we obtained the data about the rate of pit and cap formation and the simultaneous changes in Clc-EGFP fluorescence (the analysis method is explained in Fig. S1 [J–O]). Typical traces of CCP depth/cap height measured by HPICM and corresponding Clc-EGFP fluorescence intensity change are shown in Fig. 2 C. CCP formation was characterized by the rapid correlated depth (Fig. 2 D) and Clc-EGFP fluorescence (Fig. 2 F) increase with subsequent saturation. This suggests progressive clathrin recruitment during CCP invagination. Caps grew to a height of ∼160 nm above the cell surface (Fig. 2 E) and diameters similar to the diameters of CCPs being 118 ± 28 and 127 ± 19 nm, respectively. The cap growth occurred with only a small increase in Clc-EGFP fluorescence (Fig. 2, E and G) that is similar to previously published findings (Rappoport and Simon, 2003; Loerke et al., 2009) and suggests that the cap formation did not involve substantial recruitment of additional clathrin. This is also consistent with EM data (Fig. 1, C and E), which show that protrusions are not coated with clathrin. The mean pit lifetime was 72 ± 4 s ($n = 99$), and the mean cap lifetime was 44 ± 4 s ($n = 118$).

We analyzed 31 pits in Cos-7 cells transiently transfected with Abp1-EGFP and found that 23 of them closed with the formation of the cap. Among 23 pits that closed with caps, 20 pits had associated burst of Abp1-EGFP fluorescence (Fig. 2 H). The mean pit lifetime was 277.5 ± 62 s ($n = 14$), and the cap lifetime increased to 62.8 ± 12.5 s ($n = 21$). The expression of Abp1-EGFP did not affect pit depth and width.

The application of actin polymerization inhibitor, latrunculin B (40 nM), reduced the number of newly formed CCPs by 92.3% (from 1.134 pits per μm^2/h in control to 0.087 pits per μm^2/h in the presence of latrunculin B). It has also immobilized existing protrusions and prevented the formation of new pit-associated protrusions (Fig. S3, A and B). This is in good

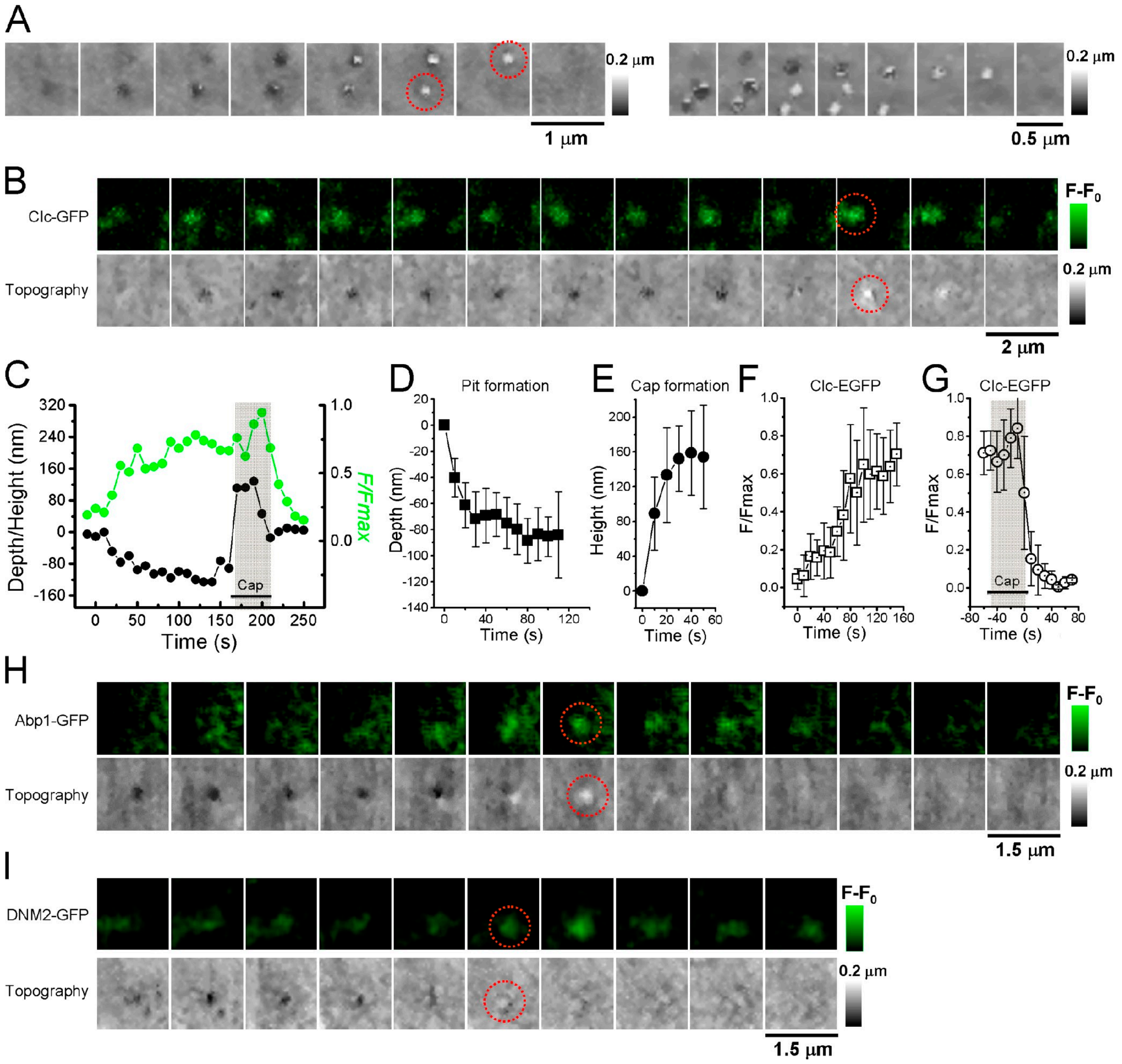

Figure 2. **Protrusion-associated CCP closure.** (A) HPICM topographical images show a cap formation process. The red circles indicate membrane protrusions associated with CCPs. (B) Topographical and fluorescent confocal image pairs show pit formation, growth, steady state, and closure. The formation of a protrusion seen in the topographical image occurs right before pit closure and disappearance of the Clc-EGFP fluorescence (red circles). (C) Example trace of typical CCP depth/cap height and corresponding Clc-EGFP fluorescence changes during pit formation, maturation, and closure with cap formation. (D) Pit depth increase during pit formation (*n* = 40). (E) Pit cap height increase during cap formation (*n* = 49). (F) Clc-EGFP fluorescence change during pit nucleation showing growth and steady state (*n* = 8). (G) Clc-EGFP fluorescence change during pit closure. The shaded region represents cap appearance before pit closure and disappearance of the Clc-EGFP fluorescence (*n* = 18). (D–G) Error bars represent SD. (H) Formation of a protrusion occurs together with the Abp1-EGFP fluorescence signal increase during pit closure (red circles). (I) Formation of a protrusion occurs together with the GFP-WT-DNM2 fluorescence increase during pit closure (red circles).

agreement with previously published observations that actin plays a variable, but not obligatory, role in receptor-mediated endocytosis (Fujimoto et al., 2000; Yarar et al., 2005). Cells transfected with Abp1-EGFP developed membrane ruffle–like structures (Fig. S2, A and C), similar to a recently reported observation (Cortesio et al., 2010).

Analysis of 34 pits in Cos-7 cells transiently transfected with the wild-type (WT) dynamin-2 (GFP-WT-DNM2) showed that the pit closure was associated with the formation of the membrane protrusions in nine cases and always correlated with the localized increase in GFP-WT-DNM2 fluorescence (Fig. 2 I). The mean pit lifetime increased to 95.3 ± 14.3 s (*n* = 20), and the cap lifetime increased to 60 ± 25.2 s (*n* = 4). The expression of WT-DNM2 did not affect pit depth and width. Cells transfected with WT-DNM2 formed dense filopodia-like structures on the apical membrane, the bases of which colocalized with WT-DNM2-GFP fluorescence spots (Fig. S2, B and D). This is in line with previously published observations that dynamin-2 and Abp1 modulate cell shape (McNiven et al., 2000). Transient transfection of cells with defective dynamin-2 EGFP (GFP-K44A-DNM2) blocked the CCP closure and increased pit lifetime to 1176.8 ± 178 s but did not influence the pit formation. Properly developed CCPs with associated GFP-K44A-DNM2 fluorescence gradually widen and flatten until fully disintegrated (Fig. S2 E). The formation of caplike protrusions was observed in some cases after the pit has flattened (Fig. S2 F). The application of a cell-permeable inhibitor of dynamin, dynasore (80 µM; Macia et al., 2006), stopped CCP dynamics in live Cos-7 cells, leaving the existing pits static on the cell surface and preventing the formation of the new pits and pit-associated protrusions (Video 4).

Analysis of CCPs that close without protrusion (cap)

The sequences of topographical images in Fig. 3 A show that pits closing with (Fig. 3 A, red circles) and without (Fig. 3 A, green circles) caps can coexist in close vicinity on the same cell. The example of CCP closure without cap formation is shown in Fig. 3 B, in which the disappearance of pit-associated Clc-EGFP fluorescence after the pit closure is delayed by ∼180 s. This is in contrast to pits that close with caps where pit-associated Clc-EGFP fluorescence disappears right after the pit closure (Fig. 2 B). Pits that do not form caps do not differ from those that form caps in their formation and closure rates, physical dimensions, and lifetimes (Fig. 3, C–H). The mean lifetime of pits that close without cap is 187.8 ± 134.2 s ($n = 65$), which is significantly longer ($P < 0.001$, compared by a two-sample unpaired Student's *t* test) than the lifetime of pits with caps (72 ± 4 s; $n = 99$).

In cells transiently transfected with Abp1-EGFP, almost all (10 out of 11) detected pits that close without caps did not have associated Abp1-EGFP fluorescence (Fig. 3 I). In cells transiently transfected with GFP-WT-DNM2, pit closure without caps was detected in 23 out of 35 analyzed pits and was associated with GFP-WT-DNM2 fluorescence increase in 20 cases (Fig. 3 J).

Regardless of whether pits form or do not form caps, they often form clusters of two and more tightly packed pits separated by 150 ± 25 nm and correlate with a more intense, larger-than-the-diffraction-limit fluorescence blobs (Fig. 1, A and B). These often had Clc-EGFP fluorescence asymmetrically distributed relative to the topographically detected pit and probably represent invaginations occurring from the edges of larger CCSs, as shown by Heuser (1980). Congruent with this, no simple linear relationship between the size of the invaginations and the fluorescence intensity of the Clc-EGFP spots could be found, which complicates the analysis of the time course of fluorescence signals.

Topographical images of pit clusters revealed that pits independently form and close within a cluster, suggesting independent regulation (Fig. S3, C and D). In 4 out of the 164 pits analyzed, pit fusion was detected (Fig. S3 E, arrows), and, in one case, a large topographically defined pit split into two smaller ones (Fig. S3 F). Splitting and fusion of clathrin-GFP fluorescence spots have also been reported (Keyel et al., 2004; Yarar et al., 2005; Kaksonen et al., 2006). Large pits were rare (6 out of 164) but had an mean lifetime of 813 ± 152 s, which is more than four times longer than the previously published lifetime of stable fluorescence clusters thought to represent large, flat clathrin arrays (Ehrlich et al., 2004). The long lifetime of pit clusters could partly be the result of a <37°C observation temperature.

Conclusions and proposed model of alternative CCP closure

Although optical microscopy techniques such as TIRF microscopy, which has also been used in combination with epifluorescent microscopy, have been reported to measure the ensemble movement of clathrin-GFP relative to the plasma membrane, they did not directly measure the topography of the cell surface (Merrifield et al., 2002; Saffarian and Kirchhausen, 2008). This study is the first direct observation of key topographical changes during the entire life cycle of individual CCPs confirmed by simultaneous fluorescent measurements. We provide new details about pit closure and clearly show that in addition to canonical symmetrical pit closure (Fig. 4, top), pits can close asymmetrically, with the formation of the protrusion at one side of the pit (Fig. 4, bottom). Although all experiments were undertaken at 28°C and therefore might reflect a particular feature elicited by the lower-than physiological temperature, both live HPICM imaging control experiments at 37°C (Fig. S1 A) and TEM images of cells fixed at 37°C (Fig. 1 C) also show the formation of a protrusion on one side of the pit. The presence of Abp1-EGFP fluorescence indicated that this protrusion contains the elements of actin cytoskeleton. The observed asymmetry may explain and support earlier published data reporting that actin fluorescence is spatially offset to Clc-GFP fluorescence (Merrifield et al., 2002; Yarar et al., 2005) and more recent findings showing rufflelike or comet tail–like patches of dendritic actin network only at one side of the CCP (Collins et al., 2011). Membrane ruffles in particular are known to participate in macropinocytosis (Doherty and McMahon, 2009). It is tempting to speculate that, despite being smaller in size, CCP closure occurs by the mechanisms similar to larger-scale phago- and macropinocytosis, although we cannot prove this based on our topographic observations alone. This argument may be strengthened by the fact that clathrin and dynamin are implicated in both CME and phago- and macropinocytosis (Liu et al., 2008; Swanson, 2008). It has been suggested that actin provides the force for movement of clathrin-coated vesicle into the cytosol (Merrifield et al., 2002; Yarar et al., 2005; Collins et al., 2011). Therefore, when pits close without a cap, the delayed disappearance of Clc-EGFP fluorescence after closure could be explained by the lack of an inward force because the connection with actin filaments had not been established. In contrast, Clc-EGFP fluorescence of pits that closed with a cap disappeared simultaneously with pit closure, suggesting actin-dependent movement. Remarkably, similar abrupt and gradual changes in clathrin intensity were previously reported (Gaidarov et al., 1999).

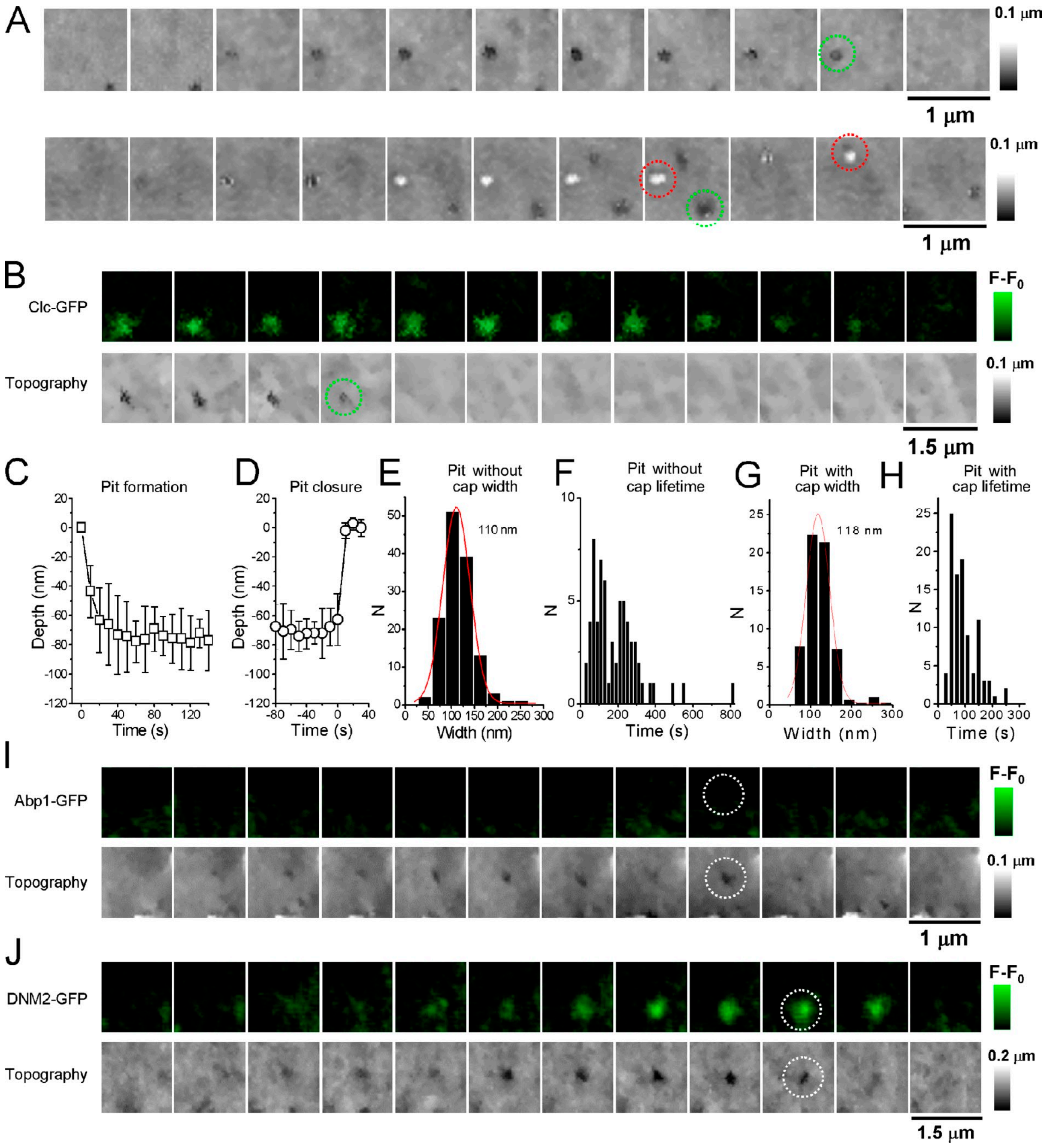

Figure 3. **Canonical CCP closure.** (A) A sequence of topographical HPICM images shows CCPs forming and closing with (red circles) and without (green circles) a cap on the same cell. (B) Topographical and fluorescent confocal image pairs show canonical CCP closure and associated Clc-EGFP fluorescence change. Clc-EGFP fluorescence remains at the pit's location ~180 s after pit closure. The green circle indicates CCP closure without membrane protrusion. (C) Depth increase during pit formation (*n* = 18). (D) Depth decrease before pit closure (*n* = 29). (C and D) Error bars represent SD. (E) Pit width distribution for pits that do not form caps (*n* = 133 from 26 independent experiments). (F) Lifetime distribution for pits that do not form caps (*n* = 65 from 26 independent experiments). (G) Pit width distribution for pits that form caps (*n* = 183 from 13 independent experiments). (H) Pit lifetime distribution for pits that form caps (*n* = 99 from 13 independent experiments). (C–H) All the data were measured using HPICM. (I) Pit closure without cap formation does not have associated Abp1-EGFP signal. White circles indicate the moment of CCP closure, as detected by ICM topography, and highlight the same area in the fluorescence confocal image where no Abp1-GFP fluorescence can be seen. (J) Pit closure without cap formation is associated with GFP-WT-DNM2 signal. White circles indicate the moment of CCP closure, as detected by ICM topography, and highlight the same area in the fluorescence confocal image where peak of DNM2-GFP intensity can be seen.

Scission of both types of pits was found to be dynamin-2 dependent, as pits failed to close in cells transfected with defective dynamin-2, and complete blockage of CME was observed in presence of the dynamin inhibitor dynasore.

The transfection of Cos-7 cells with GFP-WT-DNM2 and Abp1-EGFP induced the formation of filopodia- and rufflelike structures accordingly. Whether these protruding structures share some other molecular similarities with caps associated with CCP

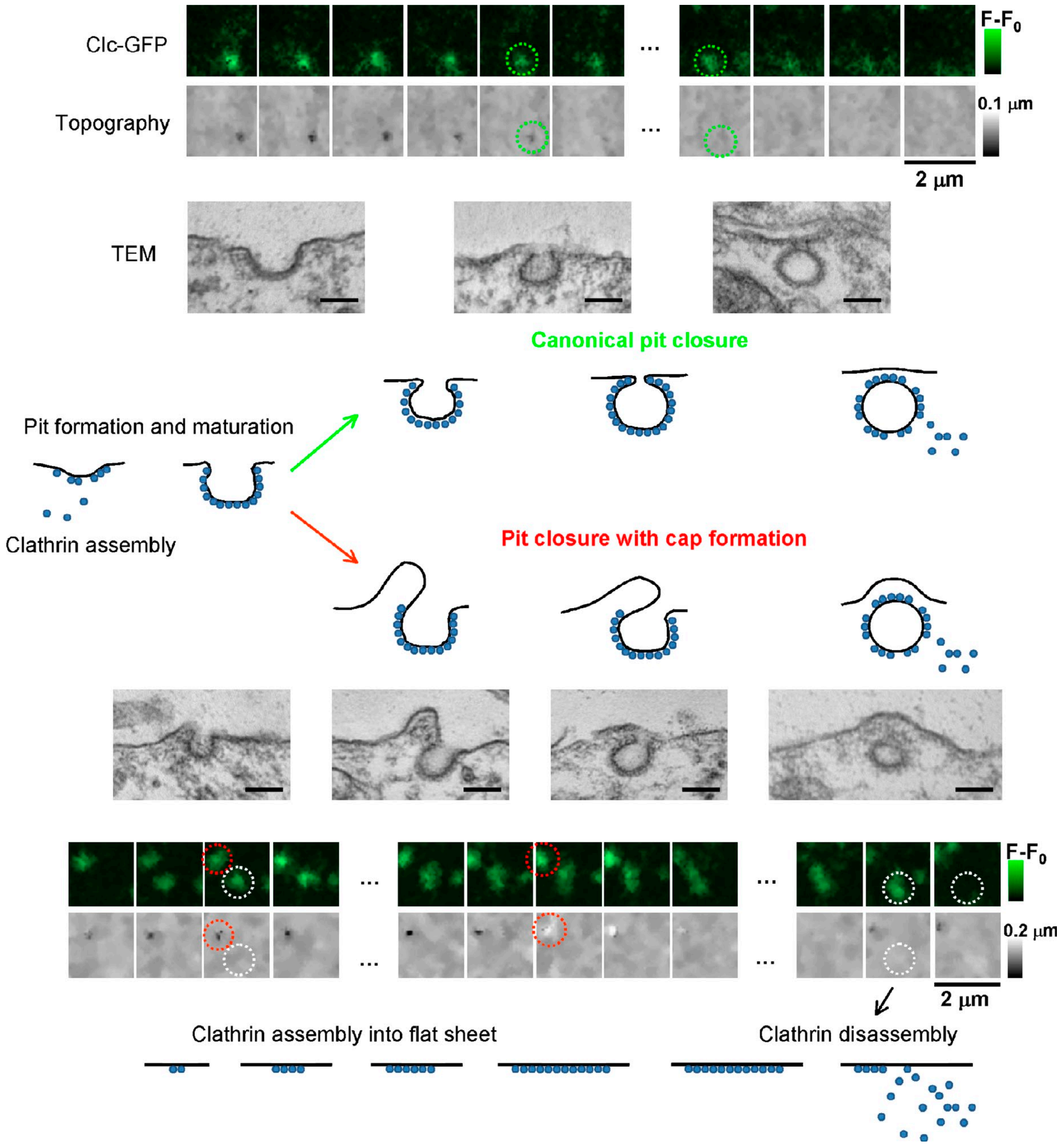

Figure 4. **Proposed model of different CCP closure types.** Clathrin molecules upon attachment to the membrane either start nucleating into a CCP or form a flat sheet. Once the CCP has gone through its maturation process, it can close with (red circles) or without (green circles) a cap. In some cases, Clc-EGFP fluorescence spots can be seen without associated topographically detected pits (white circles) that most likely represent flat sheets of clathrin. Bars, 100 µm in all TEM images.

closure that also contain dynamin-2 and Abp1 is unclear. We found that the expression of dynamin-2 reduced the proportion of pits that form caps to 26.5%, and the expression of Abp1 substantially increased pit lifetime. Additional studies would be required to understand how exactly actin regulatory and actin-binding proteins affect pit closure and the scission process and whether both types of pits support productive endocytosis.

Noteworthy is the appearance of Clc-EGFP fluorescent spots that did not result in the formation of the pit that could be detected topographically (Fig. 4, white circles). This most likely represents the assembly of a flat clathrin sheet that does not invaginate and disassembles at later stage, as suggested by the disappearing Clc-EGFP fluorescence.

Although CCS splitting and fusion have been previously reported (Keyel et al., 2004; Yarar et al., 2005), our findings show that this can also happen while a CCP is in the cell plasma membrane and not only after scission, an observation not possible with fluorescence methods alone. Our results demonstrate that fluorescence data need to be interpreted with caution, as a single diffraction-limited fluorescence spot might contain several CCPs (Fig. S3 C), as previously reported using EM (Heuser and Anderson, 1989; Yarar et al., 2005).

In the present report, we show that combined ICM–fluorescence confocal microscopy opens up possibilities for imaging the nanoscale topographical changes taking place on the apical cell surface and directly correlating these changes with the fluorescently labeled molecules, allowing key biological processes such as endocytosis, exocytosis, and viral entry to be followed at the cell surface.

Materials and methods

ICM principle of operation

ICM is a form of scanning probe microscopy that uses an electrolyte-filled glass nanopipette as an imaging probe. A sample is placed into a bath that is filled with physiological medium that also acts as an electrolyte. A bias potential is applied between the measurement electrode located inside the nanopipette, and the reference electrode is immersed in the bath. This results in an ion current flow through the pipette that drops if the pipette approaches the surface of sample. This reduction of the current can be detected when the pipette is about a radius away from the surface; thus, the vertical dimension of the sample can be measured without direct contact. The pipette is then raster scanned over the surface, and lateral and vertical positions are stored, resulting in a 3D topographical map (image). This image can be presented either as 2D with the third dimension (height) color coded (i.e., white color corresponds to highest points, and black color corresponds to lowest points; e.g., Fig. 1 A) or as a 3D projection (e.g., Fig. 1 F).

All experiments were performed using the SICM setup that is capable of better than 20-nm topographical resolution on live cells, as previously reported (Novak et al., 2009). The instrument was controlled by home-written software that was also used for data acquisition and analysis. The ICM imaging head controlled by the SICM scanner controller (Ionscope Limited) was built using the P-733.2DD XY Piezo-Nanopositioning Stage (Physik Instrumente) 30-µm travel (XY movement of the sample) and a P-753.21 piezo actuator (Physik Instrumente) 25-µm travel (Z movement of pipette). All piezos were driven by 200-W peak power low-voltage E-505 PZT amplifiers (Physik Instrumente). All piezo elements operated in capacitive sensor-controlled closed loop using the E-509 Sensor/Position Servo Control Module (Physik Instrumente). The XY piezo scanner was incorporated into a heavy stainless steel platform, which was placed onto an inverted microscope (TE2000-U; Nikon) table spring preloaded and equipped with differential micrometers (OptoSigma) for precise positioning. Coarse positioning of the pipette in the z axis was provided by an M-112.1DG translation stage with a travel range of 25 mm that was coupled with a crossed roller linear translation stage (OptoSigma) to improve stability.

The pipette current was detected via an Axopatch 200B (Molecular Devices) using a gain of 1 mV/pA and a low-pass filter setting of 5 kHz. The internal holding voltage source of the Axopatch 200B was used to supply a direct current voltage of +200 mV to the pipette. The outputs of the capacitive sensors from all three piezo elements were monitored using Axon Digidata 1322A and Clampex 9.2 (both from Molecular Devices).

To reduce the vibrations caused by the resonance of the glass pipette, a standard ESW-F10P holder (Warner Instruments) was replaced with a V-groove mounting plate where the pipette was held by a steel spring ~7 mm above the taper. Fluorescence images were recorded using the D-104 Microscope Photometer (Photon Technology International, Inc.) through a 100×/1.3 oil immersion objective. The excitation was provided by a 488-nm wavelength diode-pumped solid-state laser (Laser 200; Protera). ICM topographical and confocal fluorescence images were acquired, processed, and analyzed using ICM control and data acquisition and analysis software written by the authors.

HPICM imaging

In HPICM, at each imaging point, the pipette approaches the sample from a starting position that is above any of the surface features. The reference current is measured while the pipette is well away from the surface. The pipette then approaches until the current is reduced by a predefined amount, usually 0.25–1%. The position of the z dimension actuator when the current achieves this reduction is recorded as the height of the sample at this imaging point. All topographical HPICM images were acquired at a 32 × 32–pixel resolution; therefore, pixel sizes are as follows: 31.25 nm/pixel for a 1 × 1–µm scan; 46.875 nm/pixel for a 1.5 × 1.5–µm scan; and 62.5 nm/pixel for a 2 × 2–µm scan.

There are two major factors limiting the imaging rate in HPICM. These are the settling time of the XY piezo scanner and the rate the Z piezo brings the pipette toward the sample surface (fall rate). As highlighted in our previous paper, the hopping technique requires careful damping of mechanical vibrations that arise from the large, rapid vertical motions of the Z piezo with the attached probe (Novak et al., 2009) and the intrinsic resonances of the piezo actuators. It was possible to tune the XY piezo scanner to achieve a 5-ms settling time for a nonoscillating step response. The Z piezo response was tuned to <1 ms. At a typical fall rate used for imaging of CCPs in this paper of 80 nm/ms, the delay in the piezo response of 0.6 ms resulted in overshoot of 40 nm. This overshoot is larger than pipette diameter used for imaging (30 nm) and gets even larger with higher fall rates, making it impossible to use sharp pipettes for fast imaging in hopping mode. To compensate for this overshoot caused by the Z piezo, another piezo actuator with a 150-kHz resonant frequency and 5-µm travel (P-151.05; Physik Instrumente) was installed on top of the existing P-753.21 piezo actuator, which has a resonant frequency of 3.7 kHz. This fast, short travel piezo actuator was used only at the most critical moments when the pipette approaching the surface needed to be stopped and withdrawn rapidly; therefore, we called it the brake booster.

SICM mode of operation

In SICM, a nanopipette is mounted on a piezoelectric translation stage, and automatic feedback control moves the pipette up or down to keep the pipette current constant (the set point) while the sample is scanned in x and y directions. The position of the z dimension actuator is recorded together with x and y coordinates to build up a topographical image of the sample surface. The SICM feedback can be based on either direct current or modulated current measurements (Shevchuk et al., 2001).

ICM probes

Nanopipettes were pulled from borosilicate glass (OD of 1 mm and ID of 0.5; Intracel) using a laser-based puller (model P-2000; Sutter Instruments). The pipettes displayed resistances of ~400 MΩ (range of 300–500 MΩ.) and had an estimated inner diameter of 30 nm. The pipette inner diameters are estimated from the pipette resistance using a half cone angle of three degrees.

TIRF and fluorescence microscopy imaging and detection of individual scission events

For TIRF and fluorescence microscopy, a lens-type evanescent field microscope was used, similar in layout to that previously described (Taylor et al., 2011). In brief, the system was based on an IX70 body (Olympus), a Plan-Fluor 100×/1.45 oil M27 objective (Carl Zeiss), and an electron-multiplying charge-coupled device camera (Cascade 512B; Princeton Instruments) coupled to the microscope via a dual-view channel-splitting device (Optical Insights) for simultaneous imaging of red and green channels. The camera was driven using MetaMorph software (Molecular Devices). Focus was maintained using a PIFOC objective positioner and appropriate feedback (Physik Instrumente). Single endocytic scission events were detected using the pulsed pH assay, as previously described (Merrifield et al., 2005; Taylor et al., 2011). In brief, Cos-7 cells were transfected with mCherry fused in frame with Clc-mCherry (see Taylor et al. [2011] for details) to label CCPs and transferrin receptor fused in frame with super-ecliptic pHluorin (Tfr-phl; see Merrifield et al. [2005] for details) to detect scission events. To detect endocytic scission events, sequences of images of target cells were acquired at 0.5 Hz in conjunction with pH switching between pH 7.4 (HBS: 135 mM NaCl, 5 mM KCl, 1.8 mM $CaCl_2$, 0.4 mM $MgCl_2$, 1 mM D-(+)-glucose, 20 mM Hepes, and 2.5% FCS, adjusted to pH 7.4 with NaOH) and pH 5.5 (MBS; with same ionic composition as HBS, except that MES was used instead of Hepes) with the switch in perfusion stream triggered at the end of each camera exposure via custom transistor–transistor logic electronics. Typically, ~400 frames of data were acquired for each cell. For this study, experiments were performed at 28°C to match the temperature used for SICM experiments. Image analysis was performed as previously described (Taylor et al., 2011). In brief, complete sequences of images were deinterleaved, and the channels were separated to four separate sets of images: TfR7 (Tfr-phl images, pH 7.4), TfR5 (TfR-phl images, pH 5.5), Clc7 (Clc-mCherry images, pH 7.4), and Clc5 (Clc-mCherry images, pH 5.5). To detect scission events, bright punctae in the TfR5 image series, corresponding to newly formed endocytic vesicles, were segmented using the à trous wavelet transform (Multidimensional Image Analysis add-on to MetaMorph 6, written by V. Racine and J.-B. Sibarita, Institut Curie, Paris, France). The particle coordinate lists generated by Multidimensional Image Analysis were assembled into particle track histories in MATLAB (MathWorks) using a nearest-neighbor algorithm (track.pro, created by J.C. Crocker [Pennsylvania Muscle Institute, Philadelphia, PA] and E.R. Weeks [Emory University, Atlanta, GA]). To measure CCP lifetimes CCPs in both Clc5 and Clc7, image series were tracked, and the particle lists were combined and assembled into particle track histories in MATLAB. Bona fide scission events were mapped onto the tracked CCPs to identify scission (+) and scission (−) CCPs. All fluorescence data were extracted using custom-written MATLAB scripts, transferred, and stored in Excel worksheets (Microsoft), as previously detailed (Taylor et al., 2011).

Cell culture and plasmids

Monkey Cos-7 cells were routinely maintained at 37°C in 5% CO_2 using DME (Life Technologies) containing 5% (volume/volume) FCS. The plasmid DNA used in the experiments was pCi (Promega) containing clathrin-GFP (provided by L.E. Greene, Laboratory of Cell Biology, National Heart, Lung, and Blood Institute, National Institutes of Health, Bethesda, MD; Wu et al., 2001). The ORF of the WT DNM2 isoform 1 (available from GenBank under accession no. NM_001005360) was generated by RT-PCR from lymphocyte mRNA and inserted in frame with the GFP in pcDNA3.1/NT-GFP-TOPO (Life Technologies). The K44A plasmid was generated by directed mutagenesis using the QuikChange Site-Directed Mutagenesis Kit (Agilent Technologies). The constructed plasmids were verified by DNA sequencing.

Transfection

Cos-7 cells (1 × 106 cells per flask) were plated into a T25 flask and incubated overnight at 37°C in DME containing 5% FCS. Cells were washed before transfection with PBS, and complexes of Lipofectamine (Life Technologies) and plasmid DNA at a ratio of 1 µl to 1 µg were added in Opti-MEM (Life Technologies) without FCS to the cells. After 2 h, the media was replaced with DME containing 5% FCS. After 24 h, the cells were trypsinized and plated onto coverslips (5 × 104 per well) and incubated at 37°C overnight. Cells where then either used for live imaging or fixed for 20 min with 3% formaldehyde containing 5% sucrose.

Live-cell imaging

All topographical imaging was performed either in Leibovitz's L-15 or CO_2-independent medium (Life Technologies). Combined fluorescence and topographical imaging was performed in phenol red–free Leibovitz's L-15 medium (Life Technologies). The temperature of the medium in the bath was measured with a temperature controller (CL-100; Warner Instruments) as 28 ± 1°C. This temperature of 28°C, which is above normal room temperature, results from the heat emitted by the piezo scanner, epifluorescent attachment, and other surrounding electronic equipment. Control experiments at 37°C were performed using a temperature controller (CL-100) connected to an objective lens heating mantle (ALA Scientific Instruments).

Cell sample preparation for TEM

Cos-7 cells were fixed with 3.7% formaldehyde at 37°C. The cells were then rinsed with PBS and fixed with 2.5% glutaraldehyde overnight. The samples were postfixed in 1% osmium tetroxide for 60 min. The samples were dehydrated in 70% ethanol (2×), 90% ethanol (2×), 100% ethanol (3×), and propylene oxide (2×) at room temperature. Then, 50% araldite resin in propylene oxide was added to each well and incubated for 15 min at room temperature before changing to 100% araldite resin for a further 60 min and then kept in 100% araldite overnight. The specimens were then embedded into araldite. Ultrathin slices (0.05–0.20 µm) were cut using a microtome. The sections were stained with 1.5% uranium acetate and 5% lead citrate before viewing under a transmission electron microscope.

Online supplemental material

Fig. S1 shows a sequence of time-lapse images of CCP with a membrane protrusion appearing right before the pit closure recorded at 37°C and control TIRF recordings validating productive CME in Cos-7 cells at 28°C; the method used to calculate lifetimes of individual CCPs is also described. Fig. S2 shows cell membrane structures and their dynamics induced by the expression of Abp1-EGFP and GFP-WT-DNM2; the effect of defective dynamin DNM2-K44A-GFP on CCP lifetime and closure is also shown. Fig. S3 shows an example of the inhibitory effect of latrunculin B on CME in Cos-7 cells and independent closure of two tightly adjacent pits as well as CCP splitting and fusion. Video 1 shows time-lapse topographical SICM images of control Cos-7 cell membranes. Video 2 shows scission events manifested as the sudden appearance of TfR-phl at CCSs. Video 3 shows time-lapse topographical HPICM images of a Cos-7 cell transfected with Clc-EGFP. Video 4 shows time-lapse topographical SICM images of a Cos-7 cell membrane in the presence of a cell-permeable inhibitor of dynamin, dynasore (80 µM).

This work was supported by the Biotechnology and Biological Sciences Research Council (grant no. BBD0208751), Medical Research Council (grant no. G0700926), and British Heart Foundation (grant no. JG-NH/10/3/28574). A.I. Shevchuk, M.J. Lab, D. Klenerman, and Y.E. Korchev are founders and shareholders of Ionscope Limited.

Submitted: 28 September 2011
Accepted: 2 April 2012

References

Anderson, R.G., J.L. Goldstein, and M.S. Brown. 1976. Localization of low density lipoprotein receptors on plasma membrane of normal human fibroblasts and their absence in cells from a familial hypercholesterolemia homozygote. *Proc. Natl. Acad. Sci. USA*. 73:2434–2438. http://dx.doi.org/10.1073/pnas.73.7.2434

Bretscher, M.S., J.N. Thomson, and B.M. Pearse. 1980. Coated pits act as molecular filters. *Proc. Natl. Acad. Sci. USA*. 77:4156–4159. http://dx.doi.org/10.1073/pnas.77.7.4156

Collins, A., A. Warrington, K.A. Taylor, and T. Svitkina. 2011. Structural organization of the actin cytoskeleton at sites of clathrin-mediated endocytosis. *Curr. Biol.* 21:1167–1175. http://dx.doi.org/10.1016/j.cub.2011.05.048

Cortesio, C.L., B.J. Perrin, D.A. Bennin, and A. Huttenlocher. 2010. Actin-binding protein-1 interacts with WASp-interacting protein to regulate growth factor-induced dorsal ruffle formation. *Mol. Biol. Cell*. 21:186–197. http://dx.doi.org/10.1091/mbc.E09-02-0106

Doherty, G.J., and H.T. McMahon. 2009. Mechanisms of endocytosis. *Annu. Rev. Biochem.* 78:857–902. http://dx.doi.org/10.1146/annurev.biochem.78.081307.110540

Ehrlich, M., W. Boll, A. Van Oijen, R. Hariharan, K. Chandran, M.L. Nibert, and T. Kirchhausen. 2004. Endocytosis by random initiation and stabilization of clathrin-coated pits. *Cell*. 118:591–605. http://dx.doi.org/10.1016/j.cell.2004.08.017

Fujimoto, L.M., R. Roth, J.E. Heuser, and S.L. Schmid. 2000. Actin assembly plays a variable, but not obligatory role in receptor-mediated endocytosis in mammalian cells. *Traffic*. 1:161–171. http://dx.doi.org/10.1034/j.1600-0854.2000.010208.x

Gaidarov, I., F. Santini, R.A. Warren, and J.H. Keen. 1999. Spatial control of coated-pit dynamics in living cells. *Nat. Cell Biol.* 1:1–7. http://dx.doi.org/10.1038/8971

Hansma, P.K., B. Drake, O. Marti, S.A. Gould, and C.B. Prater. 1989. The scanning ion-conductance microscope. *Science*. 243:641–643. http://dx.doi.org/10.1126/science.2464851

Heuser, J.E. 1980. Three-dimensional visualization of coated vesicle formation in fibroblasts. *J. Cell Biol.* 84:560–583. http://dx.doi.org/10.1083/jcb.84.3.560

Heuser, J.E., and R.G. Anderson. 1989. Hypertonic media inhibit receptor-mediated endocytosis by blocking clathrin-coated pit formation. *J. Cell Biol.* 108:389–400. http://dx.doi.org/10.1083/jcb.108.2.389

Kaksonen, M., C.P. Toret, and D.G. Drubin. 2006. Harnessing actin dynamics for clathrin-mediated endocytosis. *Nat. Rev. Mol. Cell Biol.* 7:404–414. http://dx.doi.org/10.1038/nrm1940

Keyel, P.A., S.C. Watkins, and L.M. Traub. 2004. Endocytic adaptor molecules reveal an endosomal population of clathrin by total internal reflection fluorescence microscopy. *J. Biol. Chem.* 279:13190–13204. http://dx.doi.org/10.1074/jbc.M312717200

Korchev, Y.E., C.L. Bashford, M. Milovanovic, I. Vodyanoy, and M.J. Lab. 1997a. Scanning ion conductance microscopy of living cells. *Biophys. J.* 73:653–658. http://dx.doi.org/10.1016/S0006-3495(97)78100-1

Korchev, Y.E., M. Milovanovic, C.L. Bashford, D.C. Bennett, E.V. Sviderskaya, I. Vodyanoy, and M.J. Lab. 1997b. Specialized scanning ion-conductance microscope for imaging of living cells. *J. Microsc.* 188:17–23. http://dx.doi.org/10.1046/j.1365-2818.1997.2430801.x

Lack, L., and M. Gradisar. 2002. Acute finger temperature changes preceding sleep onsets over a 45-h period. *J. Sleep Res.* 11:275–282. http://dx.doi.org/10.1046/j.1365-2869.2002.00312.x

Liu, Y.W., M.C. Surka, T. Schroeter, V. Lukiyanchuk, and S.L. Schmid. 2008. Isoform and splice-variant specific functions of dynamin-2 revealed by analysis of conditional knock-out cells. *Mol. Biol. Cell*. 19:5347–5359. http://dx.doi.org/10.1091/mbc.E08-08-0890

Loerke, D., M. Mettlen, D. Yarar, K. Jaqaman, H. Jaqaman, G. Danuser, and S.L. Schmid. 2009. Cargo and dynamin regulate clathrin-coated pit maturation. *PLoS Biol.* 7:e57. http://dx.doi.org/10.1371/journal.pbio.1000057

Macia, E., M. Ehrlich, R. Massol, E. Boucrot, C. Brunner, and T. Kirchhausen. 2006. Dynasore, a cell-permeable inhibitor of dynamin. *Dev. Cell*. 10:839–850. http://dx.doi.org/10.1016/j.devcel.2006.04.002

McNiven, M.A., L. Kim, E.W. Krueger, J.D. Orth, H. Cao, and T.W. Wong. 2000. Regulated interactions between dynamin and the actin-binding protein cortactin modulate cell shape. *J. Cell Biol.* 151:187–198. http://dx.doi.org/10.1083/jcb.151.1.187

Merrifield, C.J. 2004. Seeing is believing: Imaging actin dynamics at single sites of endocytosis. *Trends Cell Biol.* 14:352–358. http://dx.doi.org/10.1016/j.tcb.2004.05.008

Merrifield, C.J., M.E. Feldman, L. Wan, and W. Almers. 2002. Imaging actin and dynamin recruitment during invagination of single clathrin-coated pits. *Nat. Cell Biol.* 4:691–698. http://dx.doi.org/10.1038/ncb837

Merrifield, C.J., D. Perrais, and D. Zenisek. 2005. Coupling between clathrin-coated-pit invagination, cortactin recruitment, and membrane scission observed in live cells. *Cell.* 121:593–606. http://dx.doi.org/10.1016/j.cell.2005.03.015

Mettlen, M., M. Stoeber, D. Loerke, C.N. Antonescu, G. Danuser, and S.L. Schmid. 2009. Endocytic accessory proteins are functionally distinguished by their differential effects on the maturation of clathrin-coated pits. *Mol. Biol. Cell.* 20:3251–3260. http://dx.doi.org/10.1091/mbc.E09-03-0256

Mettlen, M., D. Loerke, D. Yarar, G. Danuser, and S.L. Schmid. 2010. Cargo- and adaptor-specific mechanisms regulate clathrin-mediated endocytosis. *J. Cell Biol.* 188:919–933. http://dx.doi.org/10.1083/jcb.200908078

Novak, P., C. Li, A.I. Shevchuk, R. Stepanyan, M. Caldwell, S. Hughes, T.G. Smart, J. Gorelik, V.P. Ostanin, M.J. Lab, et al. 2009. Nanoscale live-cell imaging using hopping probe ion conductance microscopy. *Nat. Methods.* 6:279–281. http://dx.doi.org/10.1038/nmeth.1306

Pearse, B.M., and R.A. Crowther. 1987. Structure and assembly of coated vesicles. *Annu. Rev. Biophys. Biophys. Chem.* 16:49–68. http://dx.doi.org/10.1146/annurev.bb.16.060187.000405

Rappoport, J.Z. 2008. Focusing on clathrin-mediated endocytosis. *Biochem. J.* 412:415–423. http://dx.doi.org/10.1042/BJ20080474

Rappoport, J.Z., and S.M. Simon. 2003. Real-time analysis of clathrin-mediated endocytosis during cell migration. *J. Cell Sci.* 116:847–855. http://dx.doi.org/10.1242/jcs.00289

Saffarian, S., and T. Kirchhausen. 2008. Differential evanescence nanometry: Live-cell fluorescence measurements with 10-nm axial resolution on the plasma membrane. *Biophys. J.* 94:2333–2342. http://dx.doi.org/10.1529/biophysj.107.117234

Salisbury, J.L., J.S. Condeelis, and P. Satir. 1980. Role of coated vesicles, microfilaments, and calmodulin in receptor-mediated endocytosis by cultured B lymphoblastoid cells. *J. Cell Biol.* 87:132–141. http://dx.doi.org/10.1083/jcb.87.1.132

Shevchuk, A.I., J. Gorelik, S.E. Harding, M.J. Lab, D. Klenerman, and Y.E. Korchev. 2001. Simultaneous measurement of Ca2+ and cellular dynamics: Combined scanning ion conductance and optical microscopy to study contracting cardiac myocytes. *Biophys. J.* 81:1759–1764. http://dx.doi.org/10.1016/S0006-3495(01)75826-2

Shevchuk, A.I., G.I. Frolenkov, D. Sánchez, P.S. James, N. Freedman, M.J. Lab, R. Jones, D. Klenerman, and Y.E. Korchev. 2006. Imaging proteins in membranes of living cells by high-resolution scanning ion conductance microscopy. *Angew. Chem. Int. Ed. Engl.* 45:2212–2216. http://dx.doi.org/10.1002/anie.200503915

Shevchuk, A.I., P. Hobson, M.J. Lab, D. Klenerman, N. Krauzewicz, and Y.E. Korchev. 2008. Endocytic pathways: Combined scanning ion conductance and surface confocal microscopy study. *Pflugers Arch.* 456:227–235. http://dx.doi.org/10.1007/s00424-007-0410-4

Swanson, J.A. 2008. Shaping cups into phagosomes and macropinosomes. *Nat. Rev. Mol. Cell Biol.* 9:639–649. http://dx.doi.org/10.1038/nrm2447

Taylor, M.J., D. Perrais, and C.J. Merrifield. 2011. A high precision survey of the molecular dynamics of mammalian clathrin-mediated endocytosis. *PLoS Biol.* 9:e1000604. http://dx.doi.org/10.1371/journal.pbio.1000604

Watanabe, S., A. Punge, G. Hollopeter, K.I. Willig, R.J. Hobson, M.W. Davis, S.W. Hell, and E.M. Jorgensen. 2011. Protein localization in electron micrographs using fluorescence nanoscopy. *Nat. Methods.* 8:80–84. http://dx.doi.org/10.1038/nmeth.1537

Wu, X., X. Zhao, L. Baylor, S. Kaushal, E. Eisenberg, and L.E. Greene. 2001. Clathrin exchange during clathrin-mediated endocytosis. *J. Cell Biol.* 155:291–300. http://dx.doi.org/10.1083/jcb.200104085

Yarar, D., C.M. Waterman-Storer, and S.L. Schmid. 2005. A dynamic actin cytoskeleton functions at multiple stages of clathrin-mediated endocytosis. *Mol. Biol. Cell.* 16:964–975. http://dx.doi.org/10.1091/mbc.E04-09-0774

Zoncu, R., R.M. Perera, R. Sebastian, F. Nakatsu, H. Chen, T. Balla, G. Ayala, D. Toomre, and P.V. De Camilli. 2007. Loss of endocytic clathrin-coated pits upon acute depletion of phosphatidylinositol 4,5-bisphosphate. *Proc. Natl. Acad. Sci. USA.* 104:3793–3798. http://dx.doi.org/10.1073/pnas.0611733104